



● Technical Note

## INVESTIGATING THE ACCUMULATION OF SUBMICRON PHASE-CHANGE DROPLETS IN TUMORS

BRANDON L. HELFIELD,<sup>\*,†</sup> KIMMOON YOO,<sup>‡</sup> JINGJING LIU,<sup>‡</sup> ROSS WILLIAMS,<sup>‡</sup> PAUL S. SHEERAN,<sup>‡,§</sup>  
DAVID E. GOERTZ,<sup>‡,§</sup> and PETER N. BURNS<sup>‡,§</sup>

\* Department of Physics, Concordia University, Montreal, Canada; † Department of Biology, Concordia University, Montreal, Canada; ‡ Physical Sciences Platform, Sunnybrook Research Institute, Toronto, Canada; and § Department of Medical Biophysics, University of Toronto, Toronto, Canada

(Received 11 February 2020; revised 24 June 2020; in final from 27 June 2020)

**Abstract**—Submicron phase-change droplets are an emerging class of ultrasound contrast agent. Compared with microbubbles, their relatively small size and increased stability offer the potential to passively extravasate and accumulate in solid tumors through the enhanced permeability and retention effect. Under exposure to sufficiently powerful ultrasound, these droplets can convert into *in situ* gas microbubbles and thus be used as an extravascular-specific contrast agent. However, *in vivo* imaging methods to detect extravasated droplets have yet to be established. Here, we develop an ultrasound imaging pulse sequence within diagnostic safety limits to selectively detect droplet extravasation in tumors. Tumor-bearing mice were injected with submicron perfluorobutane droplets and interrogated with our imaging–vaporization–imaging sequence. By use of a pulse subtraction method, median droplet extravasation signal relative to the total signal within the tumor was estimated to be  $E_{\text{tumor}} = 37 \pm 5\%$  compared with the kidney  $E_{\text{kidney}} = -2 \pm 8\%$  ( $p < 0.001$ ). This work contributes toward the advancement of volatile phase-shift droplets as a next-generation ultrasound agent for imaging and therapy. (E-mail: [brandon.helfield@concordia.ca](mailto:brandon.helfield@concordia.ca)) © 2020 World Federation for Ultrasound in Medicine & Biology. All rights reserved.

**Key Words:** Acoustic droplet vaporization, Ultrasound contrast agents, Perfluorocarbon droplets, Extravasation, Enhanced permeability and retention effect, Cancer imaging, Contrast imaging.

### INTRODUCTION

Microbubble contrast-enhanced ultrasound imaging is a clinically established technique used to enhance visualization of the blood pool. This approach is commonly used in echocardiography for left ventricle opacification and myocardial perfusion estimation (Becher and Burns 2000), abdominal imaging (Wilson and Burns 2006) and antivascular therapy monitoring (Williams et al. 2011), and has recently received U.S. Food and Drug Administration (FDA) approval for pediatric imaging (Ntoulia et al. 2018). Ultrasound-driven microbubble vibrations have also been exploited to elicit therapeutic benefit (Yang et al. 2019), with applications spanning pre-clinical work on targeted nucleic acid delivery (Chen et al. 2017) via sonoporation (Bao et al. 1997;

van Wamel et al. 2006; Karshafian et al. 2009; Helfield et al. 2016), enhancing clot lysis (Datta et al. 2008; Culp et al. 2011), and recent first-in-human clinical trials initiating reversible opening of the blood–brain barrier to enhance drug delivery in amyotrophic lateral sclerosis (Abrahao et al. 2019), Alzheimer’s (Lipsman et al. 2018) and glioblastoma (Carpentier et al. 2016). One of the many advantages of contrast agent microbubbles is that their relatively large size (1–10  $\mu\text{m}$  in diameter) confines them to the intravascular space, allowing for diagnostic measurements (*e.g.*, blood flow) that would be difficult to make with diffusible tracers for other imaging modalities such as computed tomography and magnetic resonance. Their size, however, also presents a limitation for certain applications: microbubbles cannot be used to sense changes in vascular permeability, nor be associated with ligands that target sites outside the vascular system.

Phase-change perfluorocarbon (PFC) liquid droplets are an emerging class of ultrasound contrast agent.

Address correspondence to: Brandon Helfield, Department of Physics, Concordia University, L-SP-367.23, 7141 Sherbrooke Street West, Montreal, Quebec, Canada H4 B 1 R6. E-mail: [brandon.helfield@concordia.ca](mailto:brandon.helfield@concordia.ca)

Unlike traditional microbubble contrast agents, their sub-micron size and long circulation times offer the potential for passive accumulation in the interstitium of solid tumors through the enhanced permeability and retention (EPR) effect (Matsumura and Maeda 1986; Torchilin 2011). As a liquid, droplets themselves provide poor acoustic contrast and are generally not detectable at low concentrations with conventional ultrasound (Couture et al. 2006). However, when synthesized from perfluorocarbons possessing boiling points near physiologic temperature, they can be converted into detectable microbubbles approximately 5–10 times their precursor initial size *via* externally applied acoustic energy (Sheeran and Dayton 2012). Such *in situ* microbubbles have the potential to provide contrast outside the vascular compartment to detect early-stage tumors and are being investigated as a possible approach to promote efficient and targeted drug delivery through enhanced drug penetration (Rapoport et al. 2011; Ho et al. 2016) and permeabilization of nearby cellular membranes (Liu et al. 2016).

For the eventual clinical translation of this technology, droplet chemistry (*e.g.*, encapsulation material and perfluorocarbon selection [Mountford et al. 2015]) and ultrasound pulse sequence technology (*e.g.*, acoustic parameters [Li et al. 2015]) must be such that *in vivo* vaporization of submicron droplets can be performed at clinically tolerable acoustic exposure levels. While the mechanism of conversion is not fully understood, the acoustic pressure at which droplet conversion occurs, that is, the vaporization threshold, is likely a function of both intrinsic (*e.g.*, droplet properties) and extrinsic (*e.g.*, sound and its propagation medium) factors. Studies performed mostly on micron-sized droplets have reported that vaporization thresholds increase with PFC boiling point and are inversely related to droplet size (Kripfgans et al. 2000, 2004; Schad and Hynynen 2010; Shpak et al. 2014). Given these physical relationships, it has proven challenging to vaporize submicron-scale droplets *in vivo* using traditional diagnostic imaging systems. Typically, studies require two separate transducers for activation and imaging because of the specific pulse sequence requirements (*e.g.*, Kripfgans et al. 2000; Williams et al. 2013). Recently, however, studies using pre-clinical systems ( $f > 20$  MHz) and carefully formulated droplets have reported *in vivo* droplet vaporization and imaging of the resulting bubble production using imaging processing techniques on B-mode images from a single probe (Sheeran et al. 2016; Yoo et al. 2018). With a view toward clinical application within conventional transducer frequencies and output power, custom pulse sequence strategies using clinical probes and programmable systems are beginning to be explored to vaporize droplets and subsequently visualize the

resulting bubbles with non-linear, bubble-specific imaging techniques (Couture et al. 2012; Sheeran et al. 2015).

Despite the tangible progress in droplet characterization and pulse-sequence development, use of ultrasound imaging to assess submicron droplet extravasation and subsequent accumulation within the extravascular compartment remains a challenge. Here, we present an imaging strategy to estimate the extent of droplet extravasation *in vivo* using a pulse sequence that combines bubble-specific imaging and vaporization pulse sequences. The approach presented is to apply a high-powered pulse to convert droplets into microbubbles within the focal region. The newly formed microbubbles converted from intravascular droplets are expected to wash out rapidly, and fresh intravascular droplets will replace those previously vaporized. Extravascular droplets, however, are expected to be replenished at a much slower rate dictated by the EPR effect. We use this premise as the basis for determining whether droplets are situated in the extravascular compartment by repeating this combined vaporization and imaging sequence rapidly at successive time points. First, the *in vivo* droplet intravascular half-life is assessed to allow us to determine a suitable time point for droplet extravasation estimation. Next, we investigate this technique using sequential images of post-vaporization contrast to estimate droplet extravasation in both kidney and tumor environments. Finally, we compare these findings with histologic analysis.

## METHODS

### *Submicron droplet synthesis*

Submicron phase-shift perfluorobutane droplets were synthesized using a microbubble condensation strategy as described previously (Sheeran et al. 2012). Briefly, in-house phospholipid-encapsulated microbubbles were fabricated from a stock solution (1 mg/mL) of 9:1 molar ratio of 1,2-dibehenoyl-*sn*-glycero-3-phosphocholine (DBPC) and 1,2-dipalmitoyl-*sn*-glycero-3-phosphoethanolamine-*N*-(methoxy(polyethylene glycol)-5000) (DPPE-PEG5 K) (Avanti Polar Lipids, Alabaster, AL, USA). Individual samples were prepared by first transferring 1.5 mL of stock lipid solution into 3-mL glass vials. Vial headspace was exposed to vacuum for 60 min, filled with a perfluorobutane gas core (C<sub>4</sub> F<sub>10</sub>, Fluoromed, Round Rock, TX, USA) and stored at 4°C. Before each experiment, vials were allowed to equilibrate to room temperature (Helfield et al. 2012), and microbubbles were synthesized by mechanical agitation (VialMix, Lantheus Medical Imaging, Billerica, MA, USA). The microbubble vial was then inverted for 15 min at room temperature followed by removal of an aliquot of the infranatant solution. This removed large bubble outliers from the population before condensation

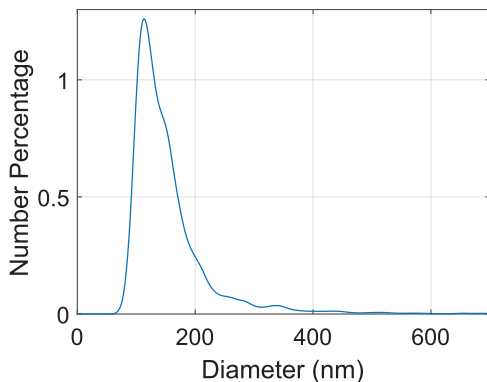


Fig. 1. Perfluorobutane droplet size distribution exhibits a peak diameter of  $114 \pm 1$  nm. Size distribution data were acquired with a NanoSite LM10 (Yoo *et al.* 2018) with a bin size of 1 nm. The peak diameter and droplet concentration ( $9.06 \pm 0.87 \times 10^{12}$  droplets/mL) are reported as the average  $\pm$  standard deviation of three vials ( $n = 3$ ). See text for synthesis details.

(Goertz *et al.* 2007). The aliquot was subsequently cooled in an isopropyl and dry-ice bath ( $-15^\circ\text{C}$ ) for approximately 1 min until visibly condensed. The resulting submicron droplet distribution (Fig. 1) was characterized by a peak diameter of  $114 \pm 1$  nm at a concentration of  $(9.06 \pm 0.87) \times 10^{12}$  droplets/mL, as measured with a NanoSite LM10 (Malvern Instruments Inc, Malvern, UK) (Yoo *et al.* 2018). Fresh droplets were synthesized on each experimental day and maintained on ice.

#### Experimental animal tumor model

Fibrosarcoma KHT-C cells (Bristow *et al.* 1990), originally derived from KHT cells (Kallman *et al.* 1967), were used in this study (obtained as a donation from Dr. Hill, University of Toronto). These cells were stored in liquid nitrogen and were cultured in Alpha MEM (No. 310-010-CL, Wisent Bioproducts) supplemented with 10% fetal bovine serum (No. 080-150, Wisent Bio-products), incubated at  $37^\circ\text{C}$  maintained at 5%  $\text{CO}_2$  and passaged twice before subculturing for tumor injections. To establish the tumor-bearing model, a  $50\text{-}\mu\text{L}$  solution of KHT-C cells at a concentration of  $7.5 \times 10^6$  cells/mL in phosphate-buffered saline was injected intramuscularly with a 27-gauge needle into both hindlimbs of 4- to 8-wk old C3 H/HeJ mice. Tumors were grown until reaching 5–8 mm in diameter. Mice were anesthetized for the duration of the experiments using 2% isoflurane and oxygen. Upon reaching study endpoints, mice were sacrificed *via* cervical dislocation under heavy anesthesia. All *in vivo* experiments were approved by the institutional animal care committee at Sunnybrook Research Institute in accordance with the Canadian Council of Animal Care.

#### Combined contrast-specific imaging and droplet vaporization pulse design

Imaging and droplet vaporization were performed using a Verasonics research platform (Verasonics, Redmond, WA, USA) equipped with a Phillips L7-4 linear array transducer operating in a focused beam mode. The Verasonics hardware was controlled *via* MATLAB scripts (The MathWorks, Natick, MA, USA). A single sequence was developed that combined a short, high-powered pulse to vaporize the submicron droplets and contrast-specific pulses to non-destructively visualize the *in situ* microbubbles. The output of the transducer in each mode was controlled by adjusting the output voltage of the Verasonics hardware, and the free-field pressure profiles were calibrated using a membrane hydrophone (400  $\mu\text{m}$ , Model 804, Sonora Medical Systems, Longmont, CO, USA) in de-gassed water. The combined sequence commenced with an amplitude-modulation pulse-inversion (AMPI) pulse train ( $f=4$  MHz, 2 cycles, mechanical index [MI] = 0.2). This three-pulse sequence consisted of a half-amplitude pulse (0.5), full-amplitude phase-inverted pulse (-1) and half-amplitude pulse (0.5), with a pulse spacing of 200  $\mu\text{s}$ . After acquisition of 20 frames of  $35 \times 40$  mm (imaging depth  $\times$  width) at a pulse repetition frequency of 20 Hz, the hardware switched to a droplet vaporization sequence with a switching time of 96 ms. The vaporization sequence consisted of a single focused pulse ( $f=5.2$  MHz, 3 cycles, MI = 1.7, beam elevation  $\sim 1.5$  mm) delivered to 26 equally spaced locations spanning 10 mm centered around the central axis of the probe at a depth of 25 mm, resulting in a duration of 5.2 ms. The hardware then automatically switched back to the AMPI imaging sequence for another 20-frame collection. The vaporization and imaging parameters were chosen as a result of *in vivo* pilot studies on mouse kidney. Mechanical indices were selected based on minimization of the high-powered MI to a level that generated consistent vaporization and sufficient microbubble contrast signal over the region of interest (ROI) while remaining within FDA safety limits. Indeed, this transmit sequence in principle mimics standard “flash” implementations on clinical scanners that switch between low and high MI pulses to image and disrupt microbubbles.

#### In vivo droplet vaporization

Experiments were performed on both healthy and tumor-bearing mice anesthetized with 2% isoflurane carried with oxygen and mounted vertically in a  $36^\circ\text{C}$  water tank immersed to the shoulder (Goertz *et al.* 2012). The abdomen (for kidneys) or hind legs (for tumors) of each mouse were shaved, treated with a depilatory cream and then cleaned. B-

Mode imaging was used to locate the organ of interest, and the imaging probe was positioned to align the location of the kidney (or tumor) at the activation focal depth of 25 mm. A 100- $\mu\text{L}$  suspension of droplets at  $9 \times 10^{12}$  droplets/mL ( $N_{\text{droplets}} \approx 10^{12}$ ) was manually injected via a 27-gauge tail vein catheter followed by a saline flush of 100  $\mu\text{L}$ .

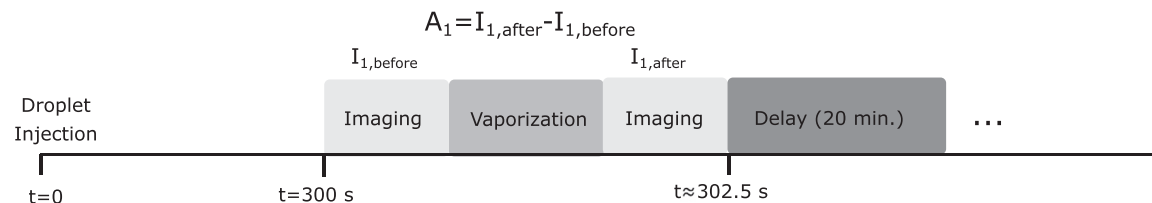
#### Circulation time experiments

To establish the *in vivo* circulation time of the droplet formulation, a subset of healthy mice ( $n=5$ ) was used to assess repeated vaporization in the kidney. Starting at 5 min post-injection, the kidney was exposed with the custom-designed pulse to trigger and image droplet vaporization every 20 min for at least 3 h (Fig. 2a). Given the average blood volume in a mouse kidney (19 mL per 100 g kidney tissue [Storey et al. 1951]) and the typical mass and size of C3H mouse kidneys ( $\sim 250$  mg, 6-mm thickness [Almajdub et al. 2008]), we estimate that the ratio of kidney blood volume to total blood volume in our mice is  $0.05/1.5 \text{ mL} \approx 3\%$ . Using the fact that our beam elevation is 1.5 mm ( $\approx 25\%$  of kidney thickness) and under the assumption that all droplets within the beam are vaporized, we estimate that  $\approx 0.8\%$  of the droplets are removed from circulation during each exposure, thus minimally confounding the measurement of droplet circulation time.

#### Extravasation experiments

To estimate droplet extravasation and accumulation within the tumor, an imaging strategy similar to that currently used for ultrasound molecular imaging (e.g., Lindner 2004) using high-MI flash imaging was adopted (Fig. 2b). After waiting sufficient time for EPR-driven droplet diffusion, the concept of this approach was to vaporize the droplets and image the resulting microbubbles within the focal region, resulting in a contrast image derived from both intravascular and any potentially extravascular droplets. Compared with the droplets situated within the intravascular space, extravasated droplets were expected to replenish at a much slower rate dependent on the EPR effect. In this work, two successive activation sequences in the same imaging plane were acquired  $\sim 30$  s apart, allowing sufficient time for the replenishment of intravascularly circulating droplets but insufficient for significant extravasation of additional droplets. Droplet extravasation was therefore quantified as the difference in contrast signal between the first vaporization sequence (extravasated + intravascular agent, referred to as  $A_1$ ) and the second vaporization sequence (intravascular agent only, referred to as  $A_2$ ). In this set of experiments on tumor-bearing mice ( $n=11$ ), we first applied this extravasation imaging sequence to the kidney at  $t_d = 15$  min post-injection as a model for a predominately “intravascular” organ, that is, one in

a) Circulation Time Protocol



b) Extravasation Imaging Protocol

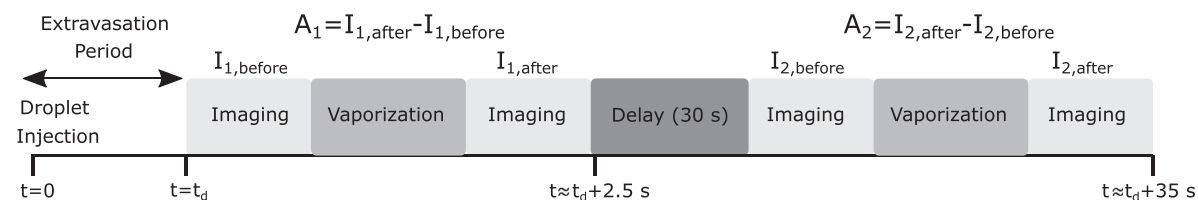


Fig. 2. Timing diagrams for both the circulation time and extravasation estimation protocols. (a) After a delay of 5 min post-droplet injection, a single combined contrast imaging and vaporization sequence is performed on the mouse kidney. The pre-vaporization image  $I_{1,\text{before}}$  is subtracted from the post-vaporization image  $I_{1,\text{after}}$ , and the resulting median echo  $A_1$  within the kidney is calculated. This is repeated every 20 min to estimate the *in vivo* circulation half-life of the droplets. (b) In either the kidney or tumor, the combined contrast imaging and vaporization sequence is performed twice in rapid succession (30 s apart), and the extravasation signal  $E$  is estimated from  $A_1$  and  $A_2$  according to Eqn (1).

which the EPR effect is absent such that very little if any extravasation of the droplets was anticipated. After the kidney was imaged, the probe was repositioned to perform the same imaging protocol on the tumor ( $t_d = 20$  min post-injection), where significant extravasation of droplets was expected.

#### *Ultrasound image analysis*

Ultrasound image analysis was performed offline in MATLAB (The MathWorks). Signal intensities were obtained from the in-phase and quadrature data, and a ROI was drawn around either the mouse kidney or tumor. For each activation sequence, the median linear echo in the ROI of the frame before the vaporization burst,  $I_{\text{before}}$ , was subtracted from that of the frame immediately after the burst,  $I_{\text{after}}$ , to assess the change in signal intensity between pre- and post-vaporization:  $A_i = I_{i,\text{after}} - I_{i,\text{before}}$  for  $i = 1$  or 2. For the first subset of experiments, the decrease in contrast captured at each time point was analyzed to obtain an estimated droplet half-life by fitting the data to an exponential decay curve. For the extravasation data set (Fig. 2b), the resulting median echo intensity from the second activation sequence  $A_2$  (~15.5 min post-injection for the kidney and ~20.5 min post-injection for the tumor) was subtracted from that of the first activation sequence  $A_1$  ( $t_d = 15$  min post-injection for the kidney and  $t_d = 20$  min post-injection for the tumor). The resulting normalized median signal intensity

$$E = \frac{A_1 - A_2}{A_1} \quad (1)$$

was thus an estimate of the proportion of the echo signal derived from extravasated droplets.

#### *Histology and image quantification*

To support the imaging findings, histology studies were performed ( $n = 4$ ) to assess the passive extravasation of a particle of similar size to the droplets within the tumor tissue in comparison to the kidney, that is, to validate that the EPR effect is present in this tumor model at  $t_d = 20$  min. Fluorescent nanobeads (FluoSpheres carboxylate-modified microspheres, 100-nm diameter, 540-nm excitation, 560-nm emission, 2% (w/v) solids, ThermoFisher Scientific F8800, Waltham, MA, USA) were employed as a sized-matched particle to our submicron droplets (peak diameter of  $114 \pm 1$  nm). The approach of using a fluorescent marker was necessary because the droplets have a limited lifetime and are not detectable on histology. A 50- $\mu\text{L}$  bolus solution of these nanobeads diluted 2:1 by volume with saline (13.33 mg/mL, resulting in  $N_{\text{beads}} \approx 1.2 \times 10^{12}$ ) was injected into tumor-bearing mice via tail-vein catheter followed by a 100- $\mu\text{L}$  saline

flush. After 20 min, fluorescent nanobeads in the systematic circulation were cleared by cardiac perfusion under anesthesia, effectively isolating extravasated beads deposited within the tissue. According to established protocols (Jordao *et al.* 2013), a 27-gauge needle was inserted into the left ventricle of the heart, and a cut was made at the right atrium. A 1% heparin solution in saline was flushed into the heart with a peristaltic pump with a flow rate of 10 mL/min. After 4 min, both kidneys and both hindlimb tumors were excised and placed in disposable tissue embedding molds (Polysciences Inc., Warrington, PA, USA) with frozen tissue sectioning compound (VWR, Richmond, IL, USA). The molds were submerged in liquid nitrogen until fully frozen and kept at  $-80^\circ\text{C}$  before cryostat sectioning. Two serial 4- $\mu\text{m}$ -thick sections were taken at three levels ( $0 \pm 500 \mu\text{m}$ ) from the center of each kidney and tumor and mounted on slides. Standard hematoxylin and eosin (H&E) staining was performed at each level, and the adjacent slices were stained with CD31 to detect blood vessels and 4',6-diamidino-2-phenylindole (DAPI) to label the cell nuclei. Epi-fluorescence images were acquired using an Olympus microscope (BX50, Olympus, Richmond Hill, ON, Canada) and an automated stager, equipped with DAPI, fluorescein isothiocyanate (FITC) and tetramethylrhodamine isothiocyanate filter cubes to image cell nuclei, endothelial cells and the fluorescent nanobeads, respectively. Regions of interest around the kidney (mean  $\pm$  standard deviation of  $0.45 \pm 0.11 \text{ cm}^2$ ) and tumor ( $0.10 \pm 0.04 \text{ cm}^2$ ) tissue were drawn under guidance from the H&E slices. Images of CD31- and FITC-labeled beads were thresholded to eliminate background, and the total positive pixel count was assessed. Extravasation was quantified based on the distribution of fluorescent beads outside and non-overlapping with CD31 signal (*i.e.*, if it were obvious that beads were on or inside a vessel, those beads were excluded from analysis). Data are presented as a nanobead index, defined as the total number of extravasated fluorescent pixels normalized by both the total CD31+ pixel count and the total area of the tissue cross-section (in  $\text{cm}^{-2}$ ). All image processing was performed using MATLAB.

#### *Statistics*

Exponential decay curves were fitted to droplet circulation data in a least-squares sense with  $R^2$  values  $>0.92$ . Statistical comparisons between kidney and tumor histology data were performed using a two-sided Student *t*-test, with  $p < 0.05$  indicating statistical significance.

## RESULTS AND DISCUSSION

The selection of an appropriate time point for extravasation studies needed to be based on a compromise between (i) intravascular droplet circulation life

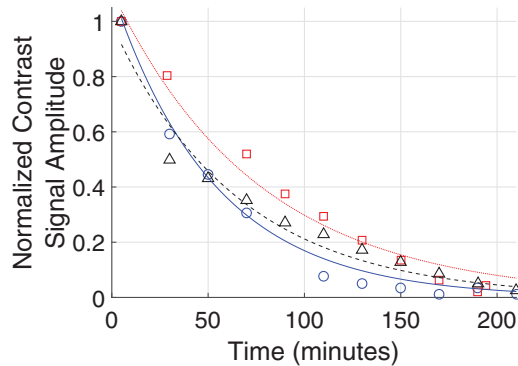


Fig. 3. *In vivo* droplet circulation half-life is sufficient for potential extravasation. Representative examples of contrast signal amplitude within a healthy mouse kidney as a function of time normalized to the first time point at 5 min (circle, triangle and square symbols) for three separate mice (blue, black and red lines). The *in vivo* droplet circulation times were extracted from an exponential decay fit (lines), resulting in a half-life of 45 ± 7 min ( $n = 5$ , reported as mean ± standard deviation).

span, (ii) allowing for sufficient time for droplet accumulation within the interstitium and (iii) droplet clearance and stability within the extravascular compartment. To address the first of these criteria, the *in vivo* circulation time of the submicron droplet formulation used in this study was assessed, resulting in a half-life of  $t_{1/2} = 45 \pm 7$  min (range: 35.7–52.5 min), as measured through serial droplet persistence within the mouse kidney ( $n = 5$ ; Fig. 3). To address the combined criteria of allowing sufficient time for droplet accumulation and minimizing extravascular droplet clearance, we conducted a small pilot study ( $n = 2$ ) using our extravasation imaging technique in mouse tumors at time points of  $t_d = 20$  and  $t_d = 70$  min post-droplet injection ( $t_{1/2} \pm 25$ ), resulting in a higher level of extravasation signal within

the tumor at  $t = 20$  min. Given this information, we proceeded to test our extravasation imaging sequence in both kidney and tumor, the results of which are illustrated in Figure 4. Representative contrast images of mouse kidney (Fig. 4a, top panel) and tumor (Fig. 4a, bottom panel) are shown after both the first and second vaporization sequences, which were separated by 30 s to allow re-filling of the intravascular compartment. The kidney images were acquired at  $t = 15$  min post-injection to account for the time required to reposition the probe such that the tumor was interrogated at  $t = 20$  min. Figure 4b depicts the global summary of our imaging results, highlighting that the percentage of estimated median extravasated signal was significantly higher in the tumor  $E_{\text{tumor}} = 37 \pm 5\%$  than in the kidney  $E_{\text{kidney}} = -2 \pm 8\%$  ( $p < 0.001$ ).

Histologic analysis was conducted using fluorescent nanobeads. Representative tissue slices revealing tissue morphology (H&E, left panels, Fig. 5) highlighted regions of healthy and cancerous tissue. Three-channel composite immunofluorescence images (middle and right panels, Fig. 5) of both kidney and tumor depict cell nuclei (dark blue), endothelial cells (green stains via CD31) and the fluorescent nanobeads (red). These images highlight the presence of nanobeads (white arrows) both adjacent to and extravasated away from blood vessel endothelial cells. The total amount of extravasated beads, taken here as red fluorescence-positive pixels that were non-overlapping with CD31+ pixels, was normalized to vessel density and ROI size. The results, illustrated in Figure 6, indicate that nanobead index was greater in the tumor  $0.24 \pm 0.09 \text{ cm}^{-2}$  compared with the kidney  $0.05 \pm 0.01 \text{ cm}^{-2}$ .

The subtraction-based imaging approach presented here extracts non-linear signal from vaporized droplets

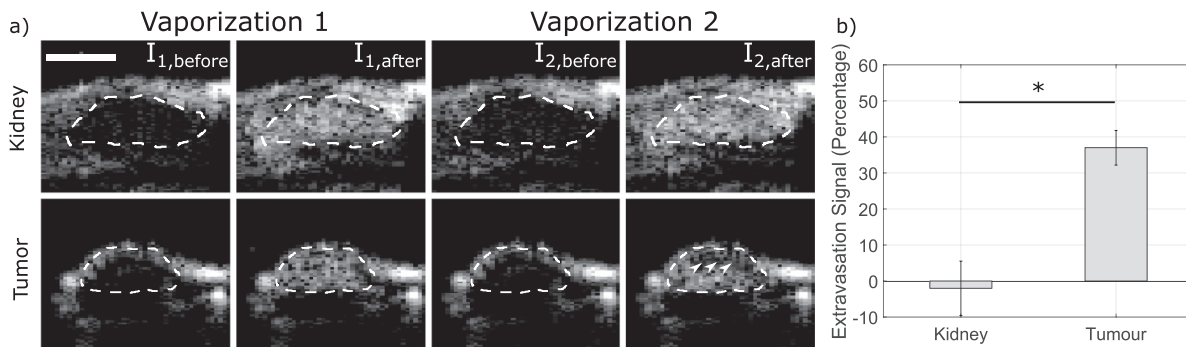
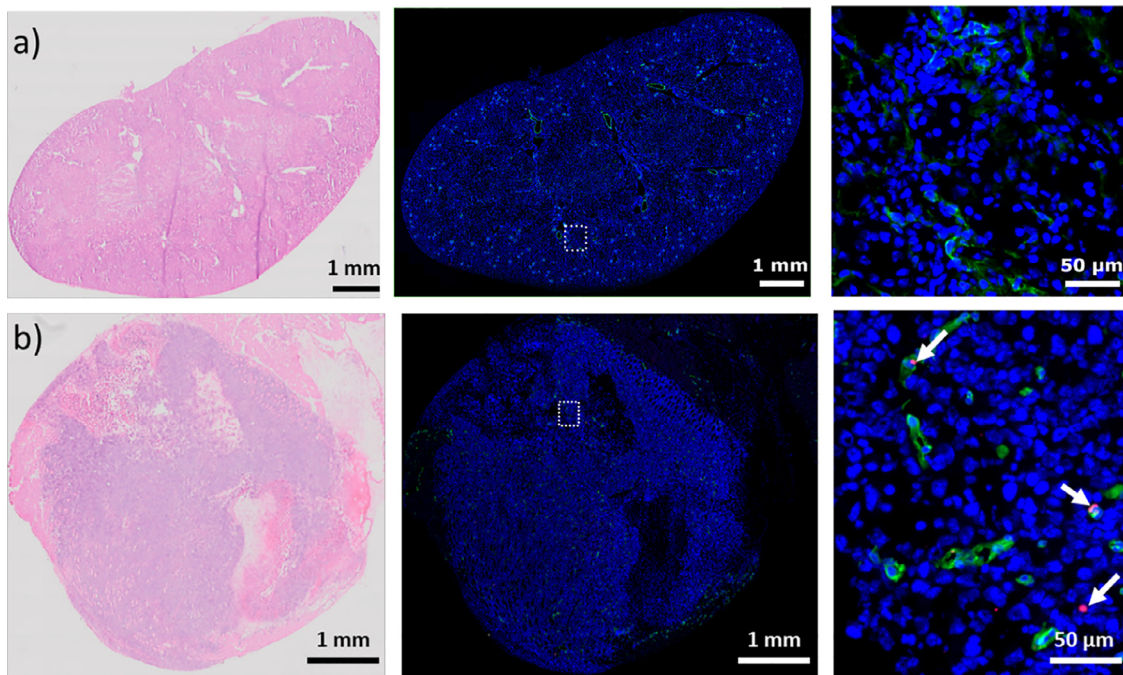


Fig. 4. Estimated droplet extravasation signal is larger in tumor than in kidney. (a) Two successive vaporization sequences (Vaporization 1 and Vaporization 2) separated by 30 s were transmitted at approximately 20 min post-droplet injection for both the kidney (highly intravascular organ) and tumor xenograft (intravascular and extravascular components) outlined by the dashed lines. The white arrowheads denote the lack of signal enhancement from the second vaporization pulse within the tumor, suggesting droplet extravasation. Bar = 5 mm. These images are log compressed with a dynamic range of 40 dB. (b) Quantification of the estimated extravasation signal (eqn [1]) from the kidney and tumor, respectively ( $n = 11$ ,  $p < 0.001$ ). Means and standard errors are displayed.



**Fig. 5.** Representative histology reveals fluorescent nanobeads in tumor samples. Histologic images of mouse (a) kidney and (b) tumor after injection of fluorescent nanobeads and a cardiac flush. Hematoxylin and eosin staining (leftmost panels) reveals gross morphology and regions of tumor tissue aiding in region-of-interest analysis. In the middle and right panels are immunofluorescence images (blue represents 4',6-diamidino-2-phenylindole [DAPI] signal for cell nuclei, green represents CD31-stained endothelial cells and red represents fluorescent nanobeads used as a surrogate measure for droplets). Right panel is a zoom-in within the *dashed white square*, and white arrows denote deposited fluorescent nanobeads.

(*i.e.*, microbubbles) that are not replenished within a 30-s time window. Previous work using ultrasound and microbubble destruction–replenishment techniques have exhibited complete tumor reperfusion in less than 30 s in both

rodent (Zhou *et al.* 2011) and clinical (Williams *et al.* 2011) tumors. Tumor blood flow, however, is known to be highly heterogeneous and comprises regions with stagnant or reverse flow (Jain 1988); vaporized droplets within these intravascular regions will appear as an artifact signal in this extravasation-specific sequence. Further, non-linear microbubble scattering is known to be affected by local confinement (Helfield *et al.* 2014), and the potential signal difference between extravascular and freely circulating microbubbles is not addressed here. Finally, the acoustic vaporization process itself may temporarily enhance the permeabilization of tumor vessels, through either the vaporization process or the subsequent microbubble cavitation (Lea-Banks *et al.* 2019). Substantial extravasation through this mechanism would result in an increase in signal intensity  $A_2$  after the 30-s time window. The net effect on our imaging sequence would be a decrease in perceived EPR-driven extravasation signal  $E$  (the subtraction of two successive vaporization sequences), changing the interpretation of our extravasation-specific estimate to a lower limit. Given this and that the results within the kidney revealed no significant extravasation signal, vaporization-induced extravasation likely does not play a major role in the interpretation of these results under the chosen conditions.

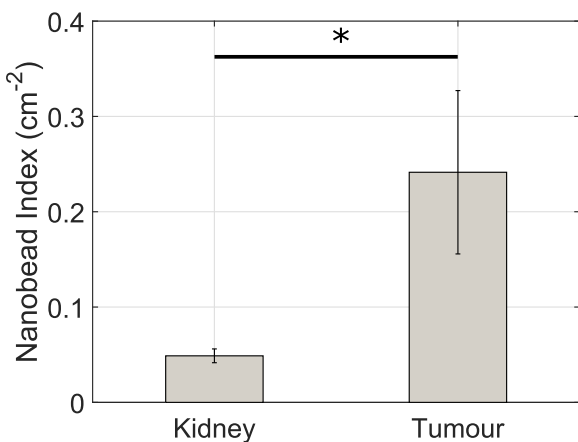


**Fig. 6.** Nanoparticle extravasation is higher in tumor than in kidney. Nanobead index is defined as the total number of extravasated fluorescent pixels normalized by both the total CD31+ pixel count and the total area of the tissue cross-section (in  $\text{cm}^{-2}$ ). This represents data from  $n=4$  mice, displayed as mean and standard error ( $p < 0.05$ ).

Our pilot data were used to determine the extravasation imaging time point ( $t_d = 20$  min). A more exhaustive evaluation of the ideal time point at which to assess passive extravasation is required to optimize this technique. Indeed, the time scale of action of EPR-driven accumulation of solid macromolecules can be as early as 10 min post-injection (Seymour 1992) and is known to be a function of particle size, surface properties, tissue type and *in vivo* surveillance mechanisms (Yuan et al. 1995; Hobbs et al. 1998; Fang et al. 2011). The optimal imaging time point  $t_d$  would be one whereby the number of extravasated droplets is maximal (*i.e.*, brightest microbubble contrast image post-vaporization). This time point is a balance between the EPR effect and subsequent extravasated particle clearance mechanisms. Lymphatic drainage is one significant mechanism involved in the clearance of solid macromolecules (Maeda et al. 2000); however, volatile droplets may in addition suffer from increased instability in the extravascular space, with even small changes in droplet size affecting vaporization thresholds (Sheeran and Dayton 2012). The stability and clearance of volatile liquid droplets from the extravascular compartment have not been directly explored, and given these complexities, further research investigating the time course of EPR of phase-shift droplets is required to select an optimal imaging time point. Finally, the vaporization process itself likely affects the resulting microbubble encapsulation (Reznik et al. 2012), which has implications in microbubble stability, vibration and scattering. The stability of these newly formed microbubbles within the extravascular compartment has not yet been explored.

It is also important to note that while the EPR effect has been well documented in small animal models, its role in clinical oncology data remains unclear. The tumor microenvironment in human cancers is more variable, resulting in a heterogeneous distribution of endothelial fenestrations and increased regions of hypoxia, which hinder this passive extravasation mechanism (Jain and Stylianopoulos 2010; Danhier 2016). While an extravascular-specific imaging technique is presented here to assess passive droplet accumulation, future work will investigate and assess the effect of microbubble-mediated sonoporation on droplet extravasation and drug penetration (*i.e.* active extravasation). Given the *in vivo* circulation time of microbubbles and the time scale of sonoporation-generated membrane permeabilization, the optimized imaging time point will likely be earlier than that suited for purely EPR-driven passive extravasation detection.

## CONCLUSIONS

Submicron phase-shift liquid droplets are an emerging class of ultrasound contrast agent with potential as an extravascular imaging tool. In this proof-of-principle study, we found an imaging technique to estimate the extent of droplet extravasation in an *in vivo* tumor model using sequential images of post-vaporization contrast. After synthesizing submicron perfluorobutane droplets, we assessed their *in vivo* half-life time, which was  $45 \pm 7$  min. We performed our imaging technique on both mouse tumors and kidneys, resulting in estimated droplet extravasation signals of  $37 \pm 5\%$  and  $-2 \pm 8\%$ , respectively. Using fluorescently labeled nanobeads, we confirmed with histology that tumor regions are characterized by enhanced retention of nanometer-sized particles compared with kidneys, a result consistent with the imaging results. This study has introduced a method to preferentially image extravasated droplets within diagnostic safety limits and thus contributes to the feasibility of volatile phase-shift droplets as a next-generation ultrasound imaging agent and therapeutic tool.

**Acknowledgments**—This study has been supported by Canadian Institutes for Health Research (CIHR) Foundation Grant MOP353808 and the National Sciences and Engineering Research Council (NSERC) Discovery Grant (B.H.). B.H. holds a Career at the Scientific Interface award from the Burroughs Wellcome Fund (BWF-CASI).

The authors thank Katerina Molnarova and Kelly Markham-Coultes for their help with the animal preparation. The authors declare no conflict of interest.

## REFERENCES

- Abraha A, Meng Y, Llinas M, Huang Y, Hamani C, Mainprize T, Aubert I, Heyn C, Black SE, Hyynen K, Lipsman N, Zinman L. First-in-human trial of blood-brain barrier opening in amyotrophic lateral sclerosis using MR-guided focused ultrasound. *Nat Commun* 2019;10:1–9.
- Almajdub M, Magnier L, Juillard L, Janier M. Kidney volume quantification using contrast-enhanced *in vivo* X-ray micro-CT in mice. *Contrast Media Mol Imaging* 2008;3:120–126.
- Bao S, Thrall BD, Miller DL. Transfection of a reporter plasmid into cultured cells by sonoporation *in vitro*. *Ultrasound Med Biol* 1997;23:953–959.
- Becher H, Burns P. Handbook of contrast echocardiography: Left ventricular function and myocardial perfusion. Frankfurt: Springer Verlag; 2000.
- Bristow RG, Hardy PA, Hill RP. Comparison between *in vitro* radiosensitivity and *in vivo* radioresponse of murine tumor cell lines: I. Parameters of *in vitro* radiosensitivity and endogenous cellular glutathione levels. *Int J Radiat Oncol Biol Phys* 1990;18:133–145.
- Carpentier A, Canney M, Vignot A, Reina V, Beccaria K, Horodyckid C, Karachi C, Leclercq D, Lafon C, Chapelon JY, Capelle L, Cornu P, Sanson M, Hoang-Xuan K, Delattre JY, Idbair A. Clinical trial of blood–brain barrier disruption by pulsed ultrasound. *Sci Transl Med* 2016;8:1–7.
- Chen HH, Matkar PN, Afrasiabi K, Kuliszewski MA, Leong-Poi H. Prospect of ultrasound-mediated gene delivery in cardiovascular applications. *Expert Opin Biol Ther* 2017;16:815–826.
- Couture O, Bevan PD, Cherin E, Cheung K, Burns PN, Foster FS. Investigating perfluorohexane particles with high-frequency ultrasound. *Ultrasound Med Biol* 2006;32:73–82.

- Couture O, Martinez L, Tabeling P. In vivo targeted delivery of large payloads with an ultrasound. *Med Phys* 2012;39:5229–5237.
- Culp WC, Flores R, Brown AT, Lowery JD, Roberson PK, Hennings LJ, Woods SD, Hatton JH, Culp BC, Skinner RD, Borrelli MJ. Successful microbubble sonothrombolysis without tissue-type plasminogen activator in a rabbit model of acute ischemic stroke. *Stroke* 2011;42:2280–2285.
- Danhier F. To exploit the tumor microenvironment: Since the EPR effect fails in the clinic, what is the future of nanomedicine? *J Control Release* 2016;244:108–121.
- Datta S, Coussios CC, Ammi AY, Mast TD, de Courten-Myers GM, Holland CK. Ultrasound-enhanced thrombolysis using definity as a cavitation nucleation agent. *Ultrasound Med Biol* 2008;34:1421–1433.
- Fang J, Nakamura H, Maeda H. The EPR effect: Unique features of tumor blood vessels for drug delivery, factors involved, and limitations and augmentation of the effect. *Adv Drug Deliv Rev* 2011;63:136–151.
- Goertz DE, de Jong N, van der Steen AFW. Attenuation and size distribution measurements of Definity and manipulated Definity populations. *Ultrasound Med Biol* 2007;33:1376–1388.
- Goertz DE, Todorova M, Mortazavi O, Agache V, Chen B, Karshafian R, Hyynen K. Antitumor effects of combining docetaxel (Taxotere) with the antivascular action of ultrasound stimulated microbubbles. *PLoS One* 2012;7:e52307.
- Helfield BL, Huo X, Williams R, Goertz DE. The effect of preactivation vial temperature on the acoustic properties of Definity™. *Ultrasound Med Biol* 2012;38:1298–1305.
- Helfield BL, Leung BYC, Goertz DE. The influence of compliant boundary proximity on the fundamental and subharmonic emissions from individual microbubbles. *J Acoust Soc Am* 2014;136:EL40–EL46.
- Helfield B, Chen X, Watkins SC, Villanueva FS. Biophysical insight into mechanisms of sonoporation. *Proc Natl Acad Sci USA* 2016;113:9983–9988.
- Ho YJ, Chang YC, Yeh CK. Improving nanoparticle penetration in tumors by vascular disruption with acoustic droplet vaporization. *Theranostics* 2016;6:392–403.
- Hobbs SK, Monsky WL, Yuan F, Roberts WG, Griffith L, Torchilin VP, Jain RK. Regulation of transport pathways in tumor vessels: Role of tumor type and microenvironment. *Proc Natl Acad Sci USA* 1998;95:4607–4612.
- Jain RK. Review Determinants of tumor blood flow: A review. *Cancer Res* 1988;48:2641–2658.
- Jain RK, Stylianopoulos T. Delivering nanomedicine to solid tumors. *Nat Rev Clin Oncol* 2010;7:653–664.
- Jordao JF, Thevenot E, Markham-Coultes K, Scarcelli T, Weng YQ, Xhima K, O'Reilly M, Huang Y, McLaurin J, Hyynen K, Aubert I. Amyloid- $\beta$  plaque reduction, endogenous antibody delivery and glial activation by brain-targeted, transcranial focused ultrasound. *Exp Neurol* 2013;248:16–29.
- Kallman RF, Silini G, van Putten LM. Factors influencing the quantitative estimation of the in vivo survival of cells from solid tumors. *J Natl Cancer Inst* 1967;39:539–549.
- Karshafian R, Bevan PD, Williams R, Samac S, Burns PN. Sonoporation by ultrasound-activated microbubble contrast agents: Effect of acoustic exposure parameters on cell membrane permeability and cell viability. *Ultrasound Med Biol* 2009;35:847–860.
- Kripfgans OD, Fowlkes JB, Miller DL, Eldevik OP, Carson PL. Acoustic droplet vaporization for therapeutic and diagnostic applications. *Ultrasound Med Biol* 2000;26:1177–1189.
- Kripfgans OD, Fabiilli ML, Carson PL, Fowlkes JB. On the acoustic vaporization of micrometer-sized droplets. *J Acoust Soc Am* 2004;116:272–281.
- Lea-Banks H, O'Reilly MA, Hyynen K. Ultrasound-responsive droplets for therapy: A review. *J Control Release* 2019;293:144–154.
- Li S, Lin S, Cheng Y, Matsunaga TO, Eckersley RJ, Tang MX. Quantifying Activation of perfluorocarbon-based phase-change contrast agents using simultaneous acoustic and optical observation. *Ultrasound Med Biol* 2015;41:1422–1431.
- Lindner JR. Molecular imaging with contrast ultrasound and targeted microbubbles. *J Nucl Cardiol* 2004;11:215–221.
- Lipsman N, Meng Y, Bethune AJ, Huang Y, Lam B, Masellis M, Herrmann N, Heyn C, Aubert I, Boutet A, Smith GS, Hyynen K, Black SE. Blood–brain barrier opening in Alzheimer's disease using MR-guided focused ultrasound. *Nat Commun* 2018;9:2336.
- Liu WW, Liu SW, Liou YR, Wu YH, Yang YC, Wang CRC, Li PC. Nanodroplet-vaporization-assisted sonoporation for highly effective delivery of photothermal treatment. *Sci Rep* 2016;6:1–14.
- Maeda H, Wu J, Sawa T, Matsumura Y, Hori K. Tumor vascular permeability and the EPR effect in macromolecular therapeutics: A review. *J Control Release* 2000;65:271–284.
- Matsumura Y, Maeda H. A new concept for macromolecular therapeutics in cancer chemotherapy: Mechanism of tumorotropic accumulation of proteins and the antitumor agent smancs. *Cancer Res* 1986;46:6387–6392.
- Mountford PA, Smith WS, Borden MA. Fluorocarbon nanodrops as acoustic temperature probes. *Langmuir* 2015;31:10656–10663.
- Ntoulia A, Anupindi SA, Darge K, Back SJ. Applications of contrast-enhanced ultrasound in the pediatric abdomen. *Abdom Radiol* 2018;43:948–959.
- Rapoport N, Nam K-H, Gupta R, Gao Z, Mohan P, Payne A, Todd N, Liu X, Kim T, Shea J, Scaife C, Parker DL, Jeong EK, Kennedy AM. Ultrasound-mediated tumor imaging and nanotherapy using drug loaded, block copolymer stabilized perfluorocarbon nanoeulsions. *J Control Release* 2011;153:4–15.
- Reznik N, Seo M, Williams R, Boleska-Pedyczak E, Lee M, Matsuura N, Gariepy J, Foster FS, Burns PN. Optical studies of vaporization and stability of fluorescently labelled perfluorocarbon droplets. *Phys Med Biol* 2012;57:7205–7217.
- Schad KC, Hyynen K. In vitro characterization of perfluorocarbon droplets for focused ultrasound therapy. *Phys Med Biol* 2010;55:4933–4947.
- Seymour LW. Passive tumor targeting of soluble macromolecules and drug conjugates. *Crit Rev Ther Drug Carrier Syst* 1992;9:135–187.
- Sheeran PS, Dayton PA. Phase-change contrast agents for imaging and therapy. *Curr Pharm Des* 2012;18:2152–2165.
- Sheeran PS, Luo SH, Mullin LB, Matsunaga TO, Dayton PA. Design of ultrasonically-activatable nanoparticles using low boiling point perfluorocarbons. *Biomaterials* 2012;33:3262–3269.
- Sheeran PS, Rojas JD, Puett C, Hjelmquist J, Arena CB, Dayton PA. Contrast-enhanced ultrasound imaging and in vivo circulatory kinetics with low-boiling-point nanoscale phase-change perfluorocarbon agents. *Ultrasound Med Biol* 2015;41:814–831.
- Sheeran PS, Daghighi Y, Yoo K, Williams R, Cherin E, Foster FS, Burns PN. Image-guided ultrasound characterization of volatile sub-micron phase-shift droplets in the 20–40 MHz frequency range. *Ultrasound Med Biol* 2016;42:795–807.
- Shpak O, Verweij M, Vos HJ, de Jong N, Lohse D, Versluis M. Acoustic droplet vaporization is initiated by superharmonic focusing. *Proc Natl Acad Sci USA* 2014;111:1697–1702.
- Storey RH, Wish L, Furth J. Organ erythrocyte and plasma volumes of tumor-bearing mice the oligemia of neoplasms. *Cancer Res* 1951;11:943–947.
- Torchilin V. Tumor delivery of macromolecular drugs based on the EPR effect. *Adv Drug Deliv Rev* 2011;63:131–135.
- van Wamel A, Kooiman K, Harteveld M, Emmer M, ten Cate FJ, Versluis M, de Jong N. Vibrating microbubbles poking individual cells: Drug transfer into cells via sonoporation. *J Control Release* 2006;112:149–155.
- Williams R, Hudson JM, Lloyd BA, Sureshkumar AR, Lueck G, Bjarnason GA, Burns PN. Dynamic microbubble contrast-enhanced us to measure tumor response to targeted therapy: A proposed clinical protocol with results from renal cell carcinoma patients receiving antiangiogenic therapy. *Radiology* 2011;260:581–590.
- Williams R, Wright C, Cherin E, Reznik N, Lee M, Gorelikov I, Foster FS, Matsuura N, Burns PN. Characterization of submicron phase-change perfluorocarbon droplets for extravascular ultrasound imaging of cancer. *Ultrasound Med Biol* 2013;39:475–489.
- Wilson SR, Burns PN. An algorithm for the diagnosis of focal liver masses using microbubble contrast-enhanced pulse-inversion sonography. *Am J Roentgenol* 2006;186:1401–1412.
- Yang C, Li Y, Du M, Chen Z. Recent advances in ultrasound-triggered therapy. *J Drug Target* 2019;27:33–50.

Yoo K, Walker WR, Williams R, Tremblay-Darveau C, Burns PN, Sheeran PS. Impact of encapsulation on in vitro and in vivo performance of volatile nanoscale phase-shift perfluorocarbon droplets. *Ultrasound Med Biol* 2018;44:1836–1852.

Yuan F, Dellian M, Fukumura D, Leunig M, Berk DA, Torchilin VP, Jain RK. Vascular permeability in a human tumor xenograft:

Molecular size dependence and cutoff size. *Cancer Res* 1995;55:3752–3757.

Zhou J, Cao L, Liu J, Zheng W, Liu M, Luo R, Han F, Li A. Quantitative assessment of tumor blood flow in mice after treatment with different doses of an antiangiogenic agent with contrast-enhanced destruction–replenishment US. *Radiology* 2011;259:406–413.